Polarization resolved H$_\alpha$ spectra from the large helical device: Emission location, temperature, and inward flux of neutral hydrogen

Atsushi Iwamae,[a] Masayuki Hayakawa, Makoto Atake, and Takashi Fujimoto
Department of Engineering Physics and Mechanics, Graduate School of Engineering, Kyoto University, Kyoto 606-8501, Japan

Motoshi Goto and Shigeru Morita
National Institute for Fusion Science, Toki 509-5292, Japan

Spectral profiles of the H$_\alpha$ line emitted from the large helical device plasma [O. Motojima *et al.*, Phys. Plasmas **6**, 1843 (1999)] have been measured with polarization-separation optics and a high-resolution spectrometer. Besides the underlying high-temperature component, which probably arises from charge-exchange recombination, the profiles are interpreted as superpositions of Zeeman profiles for two different magnetic field strengths. The emission locations are thus identified on the magnetic field map; the emissions are localized in the inner and outer regions just outside the ergodic layer, and each field-strength contribution to the overall Zeeman profile represents two radiator temperatures, and inward atom flow velocities in the range of $(1-7)\times10^3$ m/s. © *2005 American Institute of Physics.* [DOI: 10.1063/1.1855323]

I. INTRODUCTION

In the fusion-relevant magnetic confinement devices the influx of hydrogen atoms from the periphery region to the main plasma plays an important role in establishing the *H* mode and the edge thermal transport barrier.[1,2] Its quantitative estimate is required for the purpose of evaluating the particle fueling rate and controling the recycling neutrals in the long pulse discharge operation.[3,4] Information on neutral atoms has been obtained from spectroscopic measurements of the Zeeman (Paschen–Back) split profiles of lines emitted from the divertor or the periphery region in TEXTOR (Tokamak-Experiment for Technology Oriented Research),[5–8] JT-60U (Japan atomic energy research institute Tokamak-60 Upgrade),[9,10] Alcator C-Mod,[11–13] Doublet III-D,[14–16] ASDEX-U (Axially Symmetric Divertor Experiment Upgrade),[17,18] Tore Supra,[19,20] TRIAM-1M (Torus of Research Institute for Applied Mechanics) (Ref. 21) for hydrogen/deuterium, and in LHD (Large Helical Device) for helium.[22] In our earlier measurements on neutral helium,[22] the line profiles showed Zeeman structures, and they were interpreted as a superposition of two Zeeman profiles corresponding to different strengths and directions of the magnetic field on the line of sight. The locations of the He I emission were identified on the well established map of the magnetic field to be just outside the region, the so-called "ergodic layer" where the magnetic field line structure is chaotic,[2] as shown in Fig. 1(a). Figure 2 shows the H$_\alpha$ line observed under an almost identical condition. It is obvious that a similar interpretation is impractical owing to the lack of a distinctive structure. The smooth profile would be ascribed, at least partly, to the smaller Zeeman splitting of H$_\alpha$ than that of the He I λ728.1 nm (2^1P-3^1S) line and the larger Doppler broadening by a factor of 1.8 if both the species have the same temperature. In some experiments a polarizer has been used to eliminate the σ or π components of H$_\alpha$ line.[16,21] However, until now no attempt has been made in which the H$_\alpha$ line is observed with its polarized components resolved simultaneously in a toroidal device. In the following we report our polarization resolved observation.

II. EXPERIMENT

The emission from the hydrogen discharge in the LHD was observed from one of the spectroscopy ports as shown in Fig. 3. The line of sight was in the horizontal plane at a height $Z=0.026$ m, i.e., slightly above the equatorial plane; see Fig. 1(a). The cross section of the plasma is elongated in the major radius direction. In this machine the magnetic field is determined accurately by the coil currents. The magnetic field structure is saddle shaped and the field strength near the helical coil is highest. The parameters of the magnetic field vector **B** on the line of sight are plotted in Fig. 1(b)–1(d). The maximum magnetic field strength B is 2.69 T at $R=3.6$ m. The pitch angle θ which represents the angle between the direction of **B** and the horizontal plane including the line of sight is shown in (c). The yaw angle ϕ which represents the angle between the projection of **B** on the horizontal plane and the direction perpendicular to the line of sight is given in (d). (See Fig. 7 later, too.) The **B** vectors point upward in the outer region and downward in the inner region. In the inner region the yaw angle deviates substantially from zero as seen in (d). (See also Fig. 3.)

The H$_\alpha$ line emission was resolved into two orthogonally polarized components with the polarization separation optics (PSO), which is schematically shown in Fig. 4. The PSO consisted of a polarization separation Glan–Taylor prism, and a conventional Glan–Taylor prism, both of which were made of calcite, followed by a pair of lens couplers. The polarization separation Glan–Taylor prism was designed to

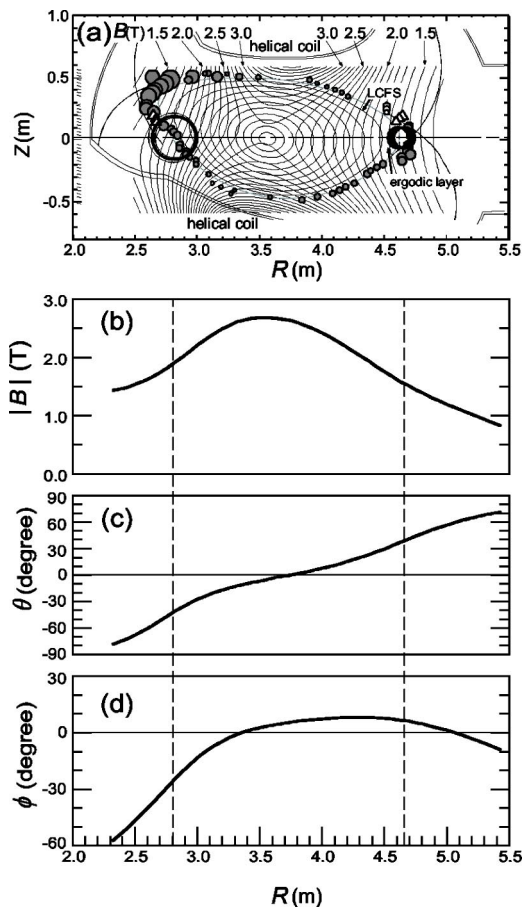---

[a]Electronic mail: iwamae@kues.kyoto-u.ac.jp

FIG. 1. (a) Map of the magnetic surfaces and field strength for the configuration of $R_{ax}=3.6$ m and $B_{ax}=2.75$ T. The R and Z axes indicate the major radial direction and the direction perpendicular to the equatorial plane, respectively. The line at $Z=0.026$ m indicates the line of sight of the present polarization separation observation. The large open circles indicate the locations of the H_α line emission and their diameters are proportional to the fitted emission intensities at the inner and outer points. The closed circles indicate the location of the He I $\lambda728.1$ nm (2^1P-3^1S) emission line reported in Ref. 22 for comparison. The diameter ratio between H_α intensity and He I intensity are arbitrary. (b) The variation of the field strength, (c) the pitch angle θ of the magnetic field from the horizontal plane, and (d) the yaw angle ϕ between the projection of the magnetic field vector on the horizontal plane and the perpendicular direction to the line of sight.

FIG. 2. An example of H_α line profiles observed without polarization separation.

FIG. 3. Top view of 1-O port of the LHD. Dotted line shows the line of sight into the plasma.

entrance surface of an optical fiber having 400 μm core diameter. The positions of the entrance surfaces of the optical fibers were carefully adjusted, and the plasma areas viewed by the both rays were confirmed to be almost identical; this was done with the He–Ne laser light. Both lines of sight had a field of view with 55, 68, and 84 mm diameters at the outer, central, and inner regions, respectively.

The optical fibers of 12 m length transmitted the light to a Czerny–Turner-type spectrometer ($f=1.33$ m) equipped with an 1800 grooves/mm grating. The slit width was 30 μm. The linearly polarized components at the input side of the optical fibers were randomized during the transmission through the optical fibers. The polarization degree of each component at the exit side of the optical fibers was less than 0.06. This residual polarization does not affect the result except for the apparent relative efficiency of the e-ray and o-ray signals even though our spectrometer has a small difference for different polarizations.

The linear dispersion was 0.3120 nm/mm at λ 656.3 nm in first order. No appreciable emission lines were found in the wavelength regions of the second and third orders. Spectra dispersed by the grating were recorded with a charge-coupled device detector, (CCD: 1024×1024 of 13 μm square pixels). The overall instrumental function was close to a Gaussian profile with a full width at half maximum 0.0115 nm or 3 pixels. A fast mechanical shutter of a 25 mm aperture was introduced on the light path in order to avoid

transmit the extraordinary ray (e ray) undeviated, and to reflect the ordinary ray (o ray) at 104° with respect to the incident light ray. The additional Glan–Taylor prism in the reflected ray eliminated the spurious e-ray component. Each of the e ray and the o ray was focused by a lens onto the
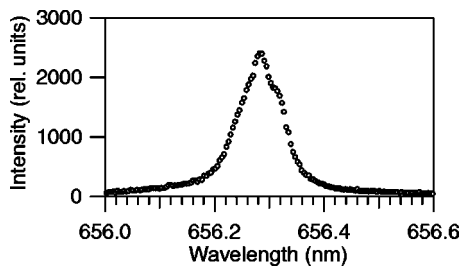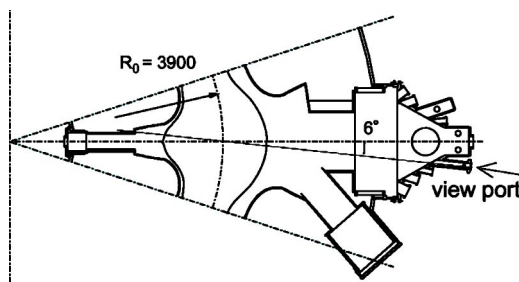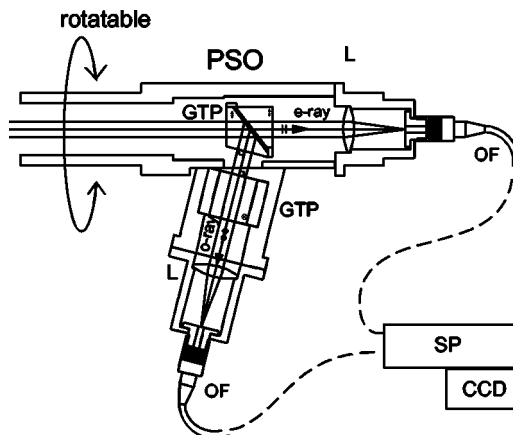

FIG. 4. Polarization separation optics (PSO). GTP: Glan–Taylor prism. L: Lens. OF: optical fiber of 400 μm core diameter. SP: Spectrometer. CCD: charge-coupled device.
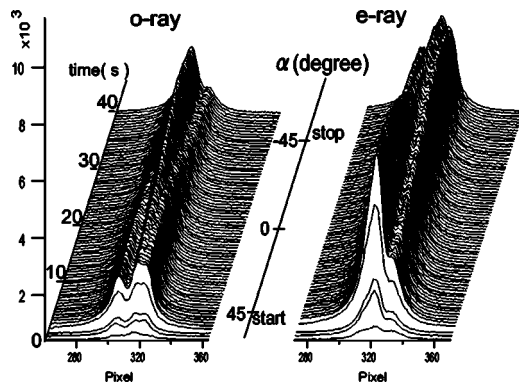
FIG. 5. Dependence of the profiles of the H$_\alpha$ line spectra separated into the e-ray and o-ray components on the rotation angle of PSO. This is for an NBI discharge plasma (shot No. 41 312).

FIG. 6. The profiles of (a) the e-ray component and (b) the o-ray component of the H$_\alpha$ line spectra (shot No. 41 292). Filled and open circles show the observed the e-ray and the o-ray intensities, respectively. Upper panels are for an NBI plasma. Lower panels are for the recombining phase after the NBI heating is turned off. Solid curves are the result of the least-squares fitting with four sets of Zeeman profiles plus a broad Gaussian profile. Thick curves are the emission from atoms in the outer region. Thin curves are the emission from atoms in the inner region. Dotted curves are the cold component. Dashed curves are the warm component. Double-dotted dashed curves are the sum of the cold and warm components. Single-dotted dashed curves are the hot component.

the smear on CCD images. The exposure time of CCD was 478 ms and the repetition frequency was 2 Hz.

The emission profile was observed during the 40 s stationary phase of hydrogen discharges heated by neutral beam injection (NBI). The input power of the NBI was ~ 600 kW. The gas-fueling rate was controlled so as to keep the line-averaged electron density $\overline{n_e}$ to be $\sim 1 \times 10^{19}$ m^{-3} and the ion temperature was $T_i \sim 1.5$ keV.

The PSO could be rotated around the axis of the line of sight during the discharge by a stepping motor which was remotely controlled. The rotation angle of PSO, α, was defined as the angle of the polarization direction of the o ray with respect to the horizontal plane. (See Fig. 7 later.) We started the rotation at $\alpha = 45°$ and stopped at $-45°$ for a NBI discharge plasma (shot No. 41 312). The time evolution of the polarization resolved spectra of H$_\alpha$ is shown in Fig. 5. The spectral profiles vary with the rotation angle of the PSO. The observed profile of the o-ray component at $\alpha = 45°$ is almost identical with that of the e-ray component at $\alpha = -45°$ and *vice versa* except for the different relative efficiency for the two rays. Both the e-ray and o-ray profiles are similar at around $\alpha = 0°$. This fact suggests that the emission is localized at inner and outer regions where the pitch angles of the magnetic field are of similar absolute values with the opposite signs (see Fig. 1). It may be interesting to note that the profiles at $\alpha \sim 0°$ look rather similar to the polarization integrated spectrum in Fig. 2.

An example of the observed H$_\alpha$ line profiles is shown in Fig. 6 at a particular angle $\alpha = -45°$; Figs. 6(a) and 6(b) shows the e-ray component and the o-ray component, respectively. The upper panels show the spectra recorded during the NBI injection. The spectra are for the time span from $t = 1.000$ to 1.478 s (shot No. 41 292).

The lower panels show the spectra in the recombining phase; in this phase the plasma shrinks to the central axis, where the magnetic field is almost in the horizontal direction. See Fig. 1(c). Both the profiles in (a) and (b) show typical normal Zeeman or Paschen–Back patterns. Since the radial motion of the plasma can be neglected in this decaying phase, the peak positions of the π components for the both rays are used for the purpose of wavelength reference for the upper panels of Fig. 6.
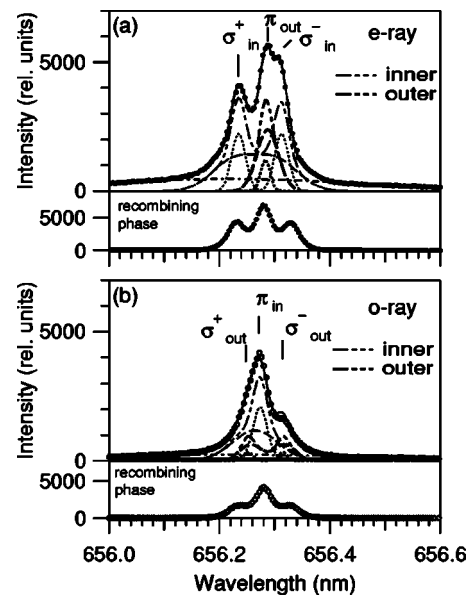
III. ANALYSIS OF THE ZEEMAN PROFILES AND DISCUSSION

The H$_\alpha$ line consists of 48 allowed and six ΔJ-forbidden Zeeman components. These are π and σ polarized. (18π and 30σ allowed, 2π and 4σ ΔJ forbidden).[5–7] The corresponding perturbed line strengths are calculated according to the method described in Ref. 23.

The π components, corresponding to $\Delta M = 0$ transitions, are linearly polarized in the plane containing the direction of observation and that of **B**. The σ^+ components correspond to $\Delta M = M_f - M_i = -1$ and are shifted to higher energy, or to the blue side of the π components. The σ^- components correspond to $\Delta M = +1$ and are shifted to the red side of the π components. If the observation direction is orthogonal to **B**, the polarization direction of σ^+ and σ^- components are perpendicular to **B**. If **B** points toward the observer, the σ^+ blue components are left-circularly polarized and the σ^- red components are right-circularly polarized. In the present experiment σ^+ and σ^- components are elliptically polarized.

Let the H$_\alpha$ line be emitted at the position O where the magnetic field **B** is directed (θ, ϕ) as shown in Fig. 7. I_π refers to the intensity which is observed from the direction in the plane perpendicular to **B**. I_σ^+ and I_σ^- are the intensities observed in the direction parallel or antiparallel to **B**. For a particular observation direction with angle ζ we define a unit vector **a** which lies along the projection of the **B** vector onto the X-Z plane. (Fig. 7). Thus **a** has Cartesian components $(\sin \eta, 0, \cos \eta)$. Then the π component is observed as the
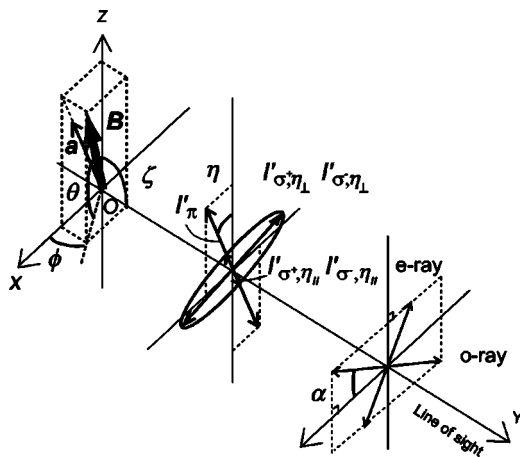
FIG. 7. The definition of the angles of the magnetic field and polarization for the line of sight as shown. θ and ϕ are the pitch and yaw angles of the magnetic field vector **B**, respectively. The observation direction at the angle ζ is defined with respect to the magnetic field. **a** is a unit vector, which lies along the projection of **B** onto the X-Z plane and η is the angle of **a** with respect to the Z axis.

light linearly polarized in the direction within the plane which includes **a** and the line of sight. We denote its intensity as I'_π

$$I'_\pi = I_\pi \sin^2 \zeta. \tag{1}$$

The σ^+ component gives rise to the intensities in both the parallel and perpendicular directions to $\mathbf{a}: I'_{\sigma^+,\eta_\parallel}$ and $I'_{\sigma^+,\eta_\perp}$, respectively:

$$I'_{\sigma^+} = I'_{\sigma^+,\eta_\parallel} + I'_{\sigma^+,\eta_\perp} \tag{2}$$

$$= \tfrac{1}{2}(\cos^2 \zeta + 1)I_{\sigma^+}, \tag{3}$$

and the σ^- component gives rise to the intensities;

$$I'_{\sigma^-} = I'_{\sigma^-,\eta_\parallel} + I'_{\sigma^-,\eta_\perp} \tag{4}$$

$$= \tfrac{1}{2}(\cos^2 \zeta + 1)I_{\sigma^-}. \tag{5}$$

The intensity observed as the o ray through the PSO with the rotation angle α, consists of the π component

$$I_{o,\pi} = I'_\pi \sin^2(\eta + \alpha) = \sin^2 \zeta \sin^2(\eta + \alpha)I_\pi \tag{6}$$

and the σ^+ and σ^- components

$$I_{o,\sigma^+} = I'_{\sigma^+,\eta_\parallel} \sin^2(\eta + \alpha) + I'_{\sigma^+,\eta_\perp} \cos^2(\eta + \alpha)$$

$$= \tfrac{1}{2}\{\cos^2 \zeta \sin^2(\eta + \alpha) + \cos^2(\eta + \alpha)\}I_{\sigma^+}, \tag{7}$$

$$I_{o,\sigma^-} = I'_{\sigma^-,\eta_\parallel} \sin^2(\eta + \alpha) + I'_{\sigma^-,\eta_\perp} \cos^2(\eta + \alpha)$$

$$= \tfrac{1}{2}\{\cos^2 \zeta \sin^2(\eta + \alpha) + \cos^2(\eta + \alpha)\}I_{\sigma^-}. \tag{8}$$

The e-ray intensity consists of the three components, $I_{e,\pi}$, I_{e,σ^+}, and I_{e,σ^-}, as given by Eqs. (6)–(8) with α replaced by $\alpha + 90°$. If no alignment nor orientation is assumed in the upper level, i.e., $I_\pi = I_{\sigma^+} = I_{\sigma^-}$, the sum of the observed polarization components,

$$I' = I'_\pi + I'_{\sigma^+} + I'_{\sigma^-}, \tag{9}$$

$$= I_{o,\pi} + I_{e,\pi} + I_{o,\sigma^+} + I_{e,\sigma^+} + I_{o,\sigma^-} + I_{e,\sigma^-} \tag{10}$$

is independent of the angle ζ.

The angles ζ and η are related to the pitch and yaw angles, θ and ϕ, of the magnetic field vectors **B**.

$$\cos \zeta = \cos \theta \sin \phi, \tag{11}$$

$$\tan \eta = \cot \theta \cos \phi. \tag{12}$$

For the purpose of fitting the experimental profiles in Fig. 6 a synthesized profile of the H_α line is constructed on the following assumptions: The H_α line is emitted at two locations, the inner and outer points on the line of sight. There are cold and warm components at each point on the line of sight. The ensemble of atoms with each temperature component moves with a certain velocity component along the line of sight. There is an additional high temperature component, represented by a broad Gaussian profile. Neither alignment nor orientation is assumed in the upper level in this fitting. In order to minimize the computation time in the least-squares fitting procedure, the central wavelength of the each component is treated in the complete Paschen–Back limit and the fine-structure splitting about 14 pm in wavelength difference is neglected. The effect of the fine structure splitting is corrected for later. We adopt the parametrization method of the Zeeman effect on the hydrogenlike spectra as discussed in Ref. 24.

Least-squares fitting was performed on the observed e-ray and o-ray line profiles simultaneously with four sets of Zeeman profiles, i.e., cold and warm components in inner and outer regions, plus a broad Gaussian profile. Each set of Zeeman profiles has an independent intensity, a Doppler width with atom temperature T_a, and a Doppler shift corresponding to the velocity component along the line of sight, v_{LOS}. The ratio of the efficiency between the e ray and the o ray is assumed to be constant within the observed wavelength range. The result of fitting of the spectra is shown in Fig. 6 with the solid curves.

Table I summarizes the parameters deduced from the fitting. From the parameter values of the magnetic field the emission locations are identified to be $R_{in} = 2.81$ m and $R_{out} = 4.66$ m. These locations are shown in Fig. 1(a) with the open circles. The diameter of the circle indicates the intensity. Also shown are similar results determined in other time windows starting at 3.5, 6.0, 8.5, 11.0, 13.5, 16.0, 18.5, and 21.0 s for the same discharge. In our previous experiment on a helium discharge, the emission locations of neutral helium lines were $R_{in} = 2.85$ m and $R_{out} = 4.70$ m on the line of sight slightly below the equatorial plane, as shown Fig. 1(a). So, the emission locations of the H_α line virtually coincide with those of the neutral helium line. The inward flow speeds of $(1 - 7) \times 10^3$ m/s are substantially higher than those estimated for helium of $\sim 1 \times 10^3$ m/s.[22]

It is worth examining the contributions from various components which make up the observed profiles in Fig. 6. The angle parameters of **B** at the inner and outer points are $\theta_{in} = -42.3°$, $\phi_{in} = -25.6°$, and $\theta_{out} = 38.7°$, $\phi_{out} = 6.4°$, respec-

TABLE I. The parameters obtained from the fitting. T_a and v_{LOS} indicate the atom temperature and the velocity along the line of sight, respectively. Asterisk (*) indicates T_a after the correction for the fine structure splitting. B, θ, and ϕ are functions of R. (shot No. 41 292; $t=1.000–1.478$ s)

	Inner		Outer		
	Cold	Warm	Cold	Warm	Hot
R(m)	2.81±0.01		4.66±0.01		⋯
B(T)	1.89		1.55		⋯
θ(deg)	−42.3		38.7		⋯
ϕ(deg)	−25.6		6.38		⋯
Intensity (10^4 relative units)	1.83±0.04	3.0±0.01	0.35±0.06	1.5±0.1	3.8±0.1
T_a(eV)	0.2±0.1*	3.2±0.1*	≤0.1*	0.68±0.07*	143±5
v_{LOS}(10^3 m/s)	3.0±0.1	7.2±0.2	−1.3±0.2	−3.2±0.2	33±2
Relative proportions (%)	17	29	4	14	39

tively. The corresponding values of ζ and η are obtained to be $\zeta_{\text{in}}=+108.6°$, $\eta_{\text{in}}=-44.7°$, and $\zeta_{\text{out}}=+85°$, $\eta_{\text{out}}=51.1°$ by Eqs. (11) and (12). According to Eqs. (6)–(8) for the o ray with $\alpha=-45°$ and the corresponding equations for the e ray, we obtain

$$I_e = \mathfrak{T}_e(0.50I_{\sigma^+,\text{in}} + 0.00I_{\pi,\text{in}} + 0.50I_{\sigma^-,\text{in}} + 0.01I_{\sigma^+,\text{out}}$$
$$+ 0.98I_{\pi,\text{out}} + 0.01I_{\sigma^-,\text{out}}) \quad (13)$$

and

$$I_o = \mathfrak{T}_o(0.05I_{\sigma^+,\text{in}} + 0.90I_{\pi,\text{in}} + 0.05I_{\sigma^-,\text{in}} + 0.495I_{\sigma^+,\text{out}}$$
$$+ 0.01I_{\pi,\text{out}} + 0.495I_{\sigma^-,\text{out}}), \quad (14)$$

where $\mathfrak{T}_e$ and $\mathfrak{T}_o$ are the efficiencies for the e ray and the o ray, respectively. It turned out that $\mathfrak{T}_e/\mathfrak{T}_o=1.91$. The $I_{\sigma^\pm,\text{in}}$ and $I_{\pi,\text{out}}$ components are dominant in the e-ray profile. $I_{\sigma^\pm,\text{out}}$ and $I_{\pi,\text{in}}$ components are dominant in the o-ray profile. This is the very reason why the present polarization resolved observation is so successful.

A spatial extent of the emission region could make the $\sigma^\pm$ components broader than the π components. In the He I case,[22] the additional broadening of the σ components of the λ 728.1 nm line was found to be smaller than 1 pm, and thus a variation of the magnetic field strength over the emission region was less than 0.05 T. This limits the extent of the emission region to be 50 mm or narrower. Since the present H$_\alpha$ profiles are complicated, it is impractical to estimate quantitatively an additional broadening of the σ components from the observed spectra. If we assume the same emission region, i.e, 50 mm or less, the additional broadening of the σ components is less than 1 pm.

Finally, we turn to the broadening expressed as "atom temperatures." In our fitting we ignored the presence of fine structure. When the Doppler width is large, our assumption is justified, but when T_a is small, the fine structure splitting of the order of 14 pm may not be neglected, and the temperature derived from our fitting may be higher than the real temperature. We include the fine-structure splitting and calculate the "phenomenological temperature" T_{fitted} against the real temperature T_{real} in the particular magnetic field strength corresponding to the inner and outer points, i.e., $B=1.89$ T and 1.55 T. Figure 8 shows an example of the results for B

$=1.89$ T. The spectral profile of the π components of the fine structure split lines with the temperature of T_{real} is fitted with a single Gaussian with the resulting temperature of T_{fitted}. At temperatures lower than 1 eV, the difference is substantial as shown in Fig. 8. We correct for the effect of fine structure which was neglected in our fitting, and deduce real temperatures from the fitted temperatures. The atom temperatures in Table I are the result after this correction is made. There are large fractional uncertainties in the temperatures of the cold components.

The present conclusion that the observed profiles consist of three components, the cold, warm, and hot components, seems to be consistent with the foregoing experiments on tokamaks.[7,9,10] Two temperature components[14,21] were also observed. In the helium experiment,[22] however, the warm components were obviously absent. We may assume that the warm component comes from molecular hydrogen: e.g., dissociated atoms from hydrogen molecules; $e+H_2\rightarrow e +2H(1s)$, 3.0 eV, those from hydrogen molecular ions; $e +H_2^+\rightarrow e+H^++H(1s)$, 4.3 eV, those due to dissociative excitation of hydrogen molecules; $e+H_2\rightarrow e+H(1s)+H(n=3)$, 7.0 eV, or those from hydrogen molecular ions; $e+H_2^+\rightarrow e +H^++H(n=2,3)$, 1.5 eV.[7,9,10,16] If this is the case, the profile should be different from the simple Gaussian shape as assumed in the present fitting. It is suggested that the cold component consists of atoms, which are released from a sur-
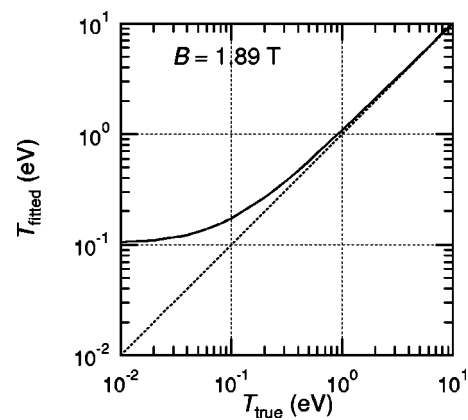

FIG. 8. Fitted temperature to a profile including the fine structure splitting.

face, having thermal energies which reflect the temperature of the emitting surface,[25] atoms produced directly by molecular dissociation; $e + H_2 \rightarrow H(1s) + H(2s)$, 0.3 eV or atoms produced through recombination of cold ions; $e + H(\text{cold}) \rightarrow H(\text{cold})$, $0.1 \sim 1$ eV. The hot component is also suggested as due to charge-exchange recombination ($20 \sim 100$ eV) and wall reflection (~ 50 eV).[7,9,10,14] This component was also present in the helium profile,[22] though the temperature was rather low, 13–20 eV.

[1] F. Wagner, G. Becker, K. Behringer *et al.*, Phys. Rev. Lett. **49**, 1408 (1982).

[2] N. Ohyabu, K. Narihara, H. Funaba *et al.*, Phys. Rev. Lett. **84**, 103 (2000).

[3] M. Sakamoto, S. Itoh, K. Nakamura, H. Zushi, H. Hanada, E. Jotaki, Y. D. Pan, S. Kawasaki, and H. Nakashima, Nucl. Fusion **42**, 165 (2002).

[4] LHD Experimental Group, M. Shoji, K. Yamazaki, A. Komori, H. Yamada, and J. Miyazawa, J. Nucl. Mater. **313-316**, 614 (2003).

[5] J. D. Hey, Y. T. Lie, D. Rusbüldt, and E. Hintz, Controlled Fusion and Plasma Physics, *Proceeding of the 21st Eur. Phys. Soc. Conf. Lisbon*, 1993.

[6] J. D. Hey, M. Korten, Y. T. Lie, A. Pospieszczyk, D. Rusbüldt, B. Schweer, B. Unterberg, J. Wienbeck, and E. Hintz, Contrib. Plasma Phys. **36**, 583 (1996).

[7] J. D. Hey, C. C. Chu, and E. Hintz, J. Phys. B **32**, 3555 (1999).

[8] J. D. Hey, C. C. Chu, Ph. Mertens, S. Brezinsek, and B. Unterberg, J. Phys. B **37**, 2543 (2004).

[9] H. Kubo, H. Takenaga, T. Sugie, S. Higashijima, S. Suzuki, A. Sakasaki, and N. Hosogane, Plasma Phys. Controlled Fusion **40**, 1115 (1998).

[10] A. Kumagai, H. Kubo, H. Takenaga, S. Suzuki, K. Shimizu, N. Asakura, and M. Shimada, Plasma Phys. Controlled Fusion **42**, 529 (2000).

[11] J. L. Weaver, B. L. Welch, H. R. Griem, J. Terry, B. Lipschultz, C. S. Pitcher, S. Wolfe, D. A. Pappas, and C. Boswell, Rev. Sci. Instrum. **71**, 1664 (2000).

[12] B. L. Welch, J. L. Weaver, H. R. Griem, W. A. Noonan, J. Terry, B. Lipschultz, and C. S. Pitcher, Phys. Plasmas **8**, 1253 (2001).

[13] J. Ghosh, H. R. Griem, R. C. Elton, J. Terry, E. Marmar, B. Lipschultz, B. LaBombard, J. E. Rice, and J. L. Weaver, Phys. Plasmas **11**, 1033 (2004).

[14] R. C. Isler, R. W. Wood, C. C. Klepper, N. H. Brooks, M. E. Fenstermacher, and A. W. Leonard, Phys. Plasmas **4**, 355 (1997).

[15] R. C. Isler, G. R. McKee, N. H. Brooks, W. P. West, M. E. Fenstermacher, and R. D. Wood, Phys. Plasmas **4**, 2989 (1997).

[16] R. C. Isler, N. H. Brooks, W. P. West, A. W. Leonard, G. R. McKee, and G. D. Porter, Phys. Plasmas **6**, 541 (1999).

[17] ASDEX Upgrade Team, T. Pütterich, R. Dux, J. Gafert, A. Kallenbach, R. Neu, R. Pungo, and S. W. Yoon, Plasma Phys. Controlled Fusion **45**, 1873 (2003).

[18] ASDEX Upgrade Team, R. Pungo, A. Kallenbach, D. Bolshukhin, R. Dux, J. Gafert, R. Neu, V. Rohde, K. Schmidtmann, W. Ullrich, and U. Wenzel, J. Nucl. Mater. **290-293**, 308 (2001).

[19] A. Escarguel, R. Guirlet, A. Azéroual, B. Pégourié, J. Gunn, T. Loarer, H. Capes, Y. Corre, C. DeMichelis, L. Godbert-Mouret, M. Koubiti, M. Mattioli, and R. Stamm, J. Nucl. Mater. **290-293**, 854 (2001).

[20] A. Escarguel, B. Pégourié, J. Hogan, C. De Michelis, Y. Corre, A. Azéroual, J. M. Ané, R. Guirlet, J. Gunn, H. Capes, L. Godbert-Mouret, M. Koubiti, and R. Stamm, Plasma Phys. Controlled Fusion **43**, 1733 (2001).

[21] T. Shikama, S. Kado, H. Zushi, A. Iwamae, and S. Tanaka, Phys. Plasmas **11**, 4701 (2004).

[22] M. Goto and S. Morita, Phys. Rev. E **65**, 026401 (2002).

[23] E. U. Condon and G. Shortley, *The Theory of Atomic Spectra* (Cambridge University Press, Cambridge, 1951).

[24] A. Blom and C. Jupén, Plasma Phys. Controlled Fusion **44**, 1229 (2002).

[25] S. Brezinsek, Ph. Mertens, A. Pospieszczyk, G. Sergienko, and U. Samm, Phys. Scr., T **T103**, 51 (2003).